Load Component Analysis of a Quad-Rotor Wind Turbine

Alexander Stillman*, Etana Ferede†, and Farhan Gandhi‡
Center for Mobility with Vertical Lift, Rensselaer Polytechnic Institute, Troy, NY, 12180, USA

A multi-rotor wind turbine consisting of 4 rotors arranged in a double-T configuration is put through a series of test cases to analyze the vibratory loads. The turbines are 4 x 1.5MW, 70m rotor diameter turbines taken from the NREL WINDPACT 1.5-70 baseline model. The test cases include rigid booms and tower without tower and boom shadow, flexible booms and a rigid tower without tower and boom shadow, flexible booms and a rigid tower with tower and boom shadow, and flexible booms and tower with tower and boom shadow. The magnitudes of the vibratory loads for each case are found and the sources of the loads are determined. It is found that the inertial loads dominate the loads without tower and boom shadow. When the booms are flexible, the magnitudes of the vibratory loads from the left and right booms differ by nearly 2x due to an asymmetrical gyroscopic torque generated by the co-rotating rotors at the tips of the booms. The flexible booms also increase the magnitude of the loads up to 25x for the force in the thrust direction. When tower and boom shadow are implemented, the vibratory loads increase by up to 11x for the side force. Tower and boom shadow act as an impulse in the aerodynamic loading, increasing the higher frequency content of the load components. Under the effect of tower and boom shadow, the aerodynamic component of the loads becomes the largest component of the loads. The impact of shadow is decreased when the size of the shadow is decreased by changing either the boom's aerodynamic shape or size, leading to a reduction of up to 66% in the magnitude of the loads when the boom is 60% of the baseline diameter. When the tower is flexible, there is interaction between the top and bottom rotors and yaw bearing loads. This leads to an increase in the magnitude of the loads of up to 3x for the side force.

I. Introduction

Wind energy continues to expand as the desire to replace current methods of electricity generation for renewable methods of energy generation grows. There is incentive to find innovative technologies and processes that reduce the Levelized Cost of Energy (LCOE), a measurement of the success of generating electricity from wind compared to other energy sources. Reducing LCOE will make wind energy more competitive in power generation against currently established practices. The multi-rotor turbine concept (where multiple rotors are mounted onto a single tower) seeks to offer an alternative method for scaling power generation instead of just increasing the size of a single rotor. Multi-rotor turbines benefit from the cheaper components of smaller systems while retaining the swept area and power gain of a larger single rotor turbine.

Multi-rotor turbines date back to the early 19th century. A Danish wind mill was modified into a twin-rotor wind mill [1]. The first multi-rotor wind turbine designed to produce electricity was proposed in 1932 [2]. In the late 20th century, the Dutch company Lagerway constructed and operated multiple multi-rotor turbines [3]. NASA Langley wind tunnel in Virginia tested a multi-rotor wind turbine consisting of seven rotors on a single frame in 2010 [3]. In 2016, Vestas Wind Energy Systems A/S built and tested a quad-rotor wind turbine consisting of four, three bladed V29-225KW rotors mounted onto one tower [4]. Multiple studies have been done on the aerodynamic properties of a multi-rotor wind turbine. Some of these studies focus the structure of the wakes produces by multi-rotor wind turbines [4–6]. There have also been studies into the overall power production and aerodynamic performance of multi-rotor turbines compared to single rotor turbines [7, 8]. A variety of studies investigate instability and perform modal analyses on multi-rotor turbines [9–11] and there has been examination of fatigue on multi-rotor turbines [12, 13].

One area of research that has not been heavily investigated is the vibratory loads present on a multi-rotor turbine. The designs of multi-rotor turbines introduce additional sources of vibratory loads in the form of additional rotors and large, horizontal booms. These structures are not present on single rotor towers and they present new dynamic loads that

*Graduate Research Assistant, Center for Mobility with Vertical Lift (MOVE).
†Research Scientist, Center for Mobility with Vertical Lift.
‡Redfern Chair Professor and MOVE Director, Center for Mobility with Vertical Lift, AIAA Fellow.

need to be accounted for in the design of the turbine. This paper investigates the vibratory loads of a quad-rotor turbine, looking at the magnitude of the loads and identifying their sources.

II. Methodology

A multirotor turbine is modeled using SIMPACK [14], a multibody simulation software, coupled with Aerodyn V15, an open source software from NREL [15] that calculates the aerodynamic blade loads. SIMPACK uses rigid and flexible bodies to analyze the non-linear response of multibody systems. The quadrotor turbine that is analyzed is shown in Figure 1. It is modeled as a double-T with 4 identical rotors. The turbine is upwind-facing. There are no cables or forward sweep of the booms. The nacelles have a rigid connection to the boom. The tower is 136.75 m tall. It has an outer diameter of 4.3 m for 70% of its height and linearly tapers to 3.7 m. The booms are 36.75 m long with an outer diameter that tapers from 3.4 m to 2.6 m. The top and bottom booms have a vertical separation of 73.5 m. The nacelle is offset from the boom axis vertically by 2.45 m. The minimum rotor separation distance is set to 5% of the rotor diameter [4]. The tower and booms are hollow cylinders with a Young's modulus of $2.1 \cdot 10^{11}\ N/m^2$ and a density of 8100 $kg/m^3$3. The tower, booms, and blades can be modeled as rigid or elastic bodies; with the effect of tower and boom elasticity explored in the results section. The elastic tower deformation is modeled with a linear combination of the first two fore-aft and side-side modes with the first torsion mode. The boom deformation is modeled with the first fore-aft, up-down, and torsion modes. The fore-aft mode is movement of the tip in the x-direction, the up-down movement of the tip is in the vertical direction, and torsion is rotation about the axis of the boom. The elastic blades are modeled as torsionally rigid and use the first two flap modes and the first lag mode. The tower foundation is modeled using a clamped boundary condition. The salient properties of the turbine are shown in Table 1.

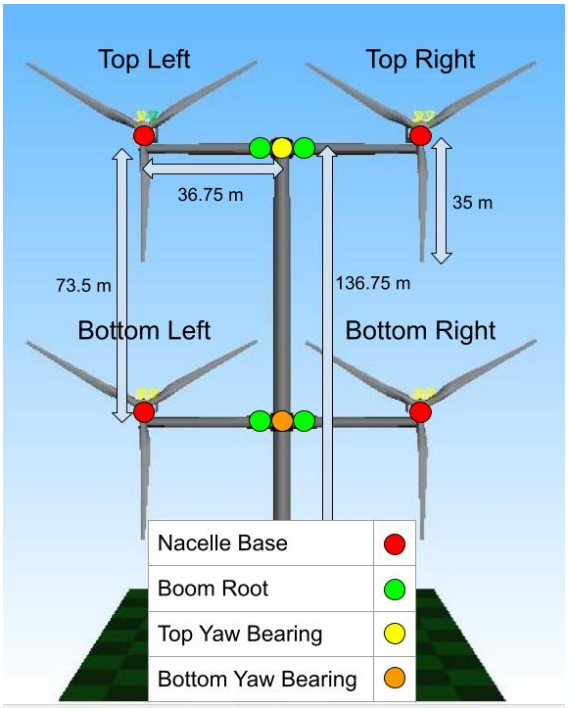

Fig. 1 Turbine Model with Locations Identified

Aerodynamic loads are calculated in AerodynV15 with Blade Element Momentum Theory (BEMT) and are passed to SIMPACK. The model implements a wind shear gradient. A correction is formulated to account for the effect of tower and boom shadow on axial inflow. The velocity deficit from shadow is corrected with Equation 1 [16]

$$\frac{u}{u_\infty} = (1 - \frac{0.25D^2(x^2 - y^2)}{(x^2 + y^2)^2}) \tag{1}$$

where u_∞ is the undisturbed incoming axial velocity, D is the tower or boom diameter, x is the distance between the

Table 1 Gross Properties for Quad-rotor Wind Turbine [12]

Parameter	Value
Rating(MW)	4x1.5
Control	Var Speed, Coll. Pitch
Rotor, Hub Diameter(m)	70, 3.5
Hub Height(m)	136.75(top) / 63.25(bottom)
Rated Wind Speed(m/s) (Top Rotors)	11.4
Rated Rotor Speed(rpm) (Top Rotors)	21.8
Rated Tip Speed(m/s)	80
Overhang(m), Shaft Tilt(deg), Precone(deg)	3.3, 0, 2.5

rotor plane and the support structure, and y is the distance from the axis of symmetry through the tower and boom center line. The adjusted velocity field is calculated to account for shadow and wind shear by multiplying the wind shear gradient field with the velocity deficit correction due to shadow. This process is detailed in Figure 2 which shows how the wind shear and tower and boom shadow are combined to generate the wind field. The torque and pitch controller are implemented in Simulink by receiving, as input, the rotor speed and collective pitch angle for each rotor from SIMPACK and passing the generator and collective pitch torque to SIMPACK. The turbine is controlled using a non-optimal generator torque when operating at below-rated speed and by a variable-speed collective pitch-to-feather controller when operating above the rated speed [12].

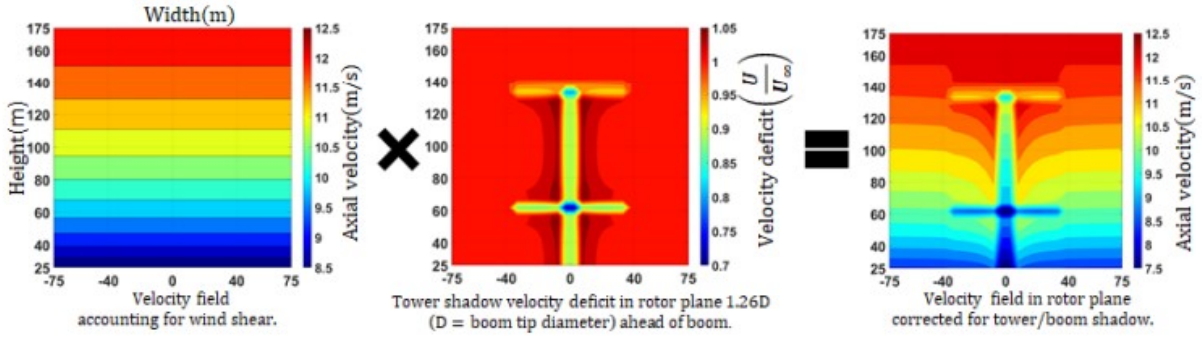

Fig. 2 Correction for Tower and Boom Shadow [12]

Figure 3 defines the directions of the loads at the top yaw bearing. These definitions are kept consistent for the booms and rotor loads. The vibratory load F_x acts along the direction of thrust, the vibratory load F_y acts along the boom axis, and the vibratory load F_z acts along the vertical axis and is positive up. The moments act about their corresponding axes and are positive counter-clockwise. The moment M_x is yaw bearing roll moment, the moment M_y is the yaw bearing pitching moment, and the moment M_z is the yaw bearing yaw moment.

This study will analyze the vibratory forces and moments for specific load conditions on the tower. The loads will be decomposed to determine the sources of the loads and understand any unusual effects caused by aspects of the tower and booms. The following results concern the case of steady wind with a wind shear gradient. The velocity is set to 11 m/s at the top rotors with a wind shear exponent of 0.2. The rotor blades are kept flexible throughout each simulation while the flexibility of the booms and tower are modified to observe the effects of support structure flexibility on the vibratory loads. Shadow is similarly altered to isolate its effect on the vibratory loads. The pertinent load cases are classified as:

1) Rigid tower and booms, without tower and boom shadow
2) Flexible booms, rigid tower, without tower and boom shadow
3) Flexible booms, rigid tower, with correction for tower and boom shadow
4) Flexible booms and tower, with and without correction for tower and boom shadow

The primary points of interest of the turbine are the yaw bearings, identified in Figure 1. This is where the booms attach to the tower and the yaw bearing experiences the summation of the vibratory loads coming from the left and right

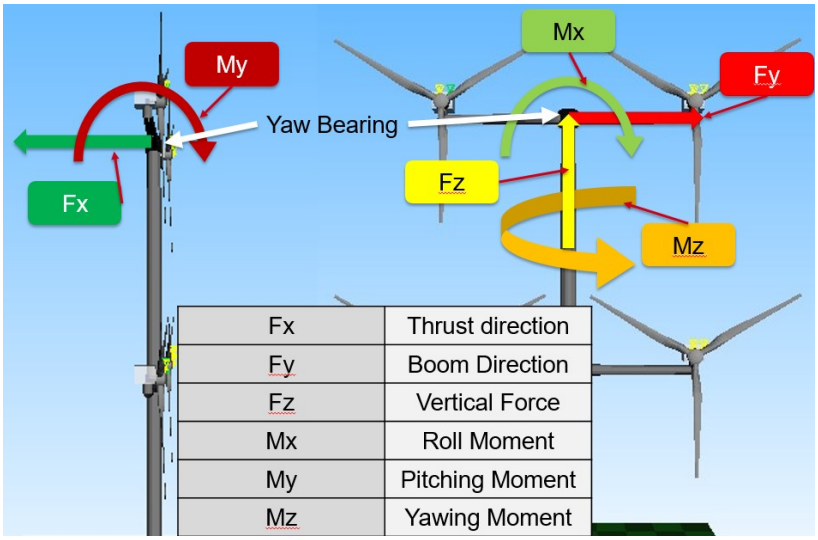

Fig. 3 Force and Moment Directions

booms. For the cases where the tower is rigid, results will be shown primarily for the top yaw bearing, booms, and rotors as the rigid tower isolates the loads from the top rotor from the loads of the bottom rotors. When tower flexibility is implemented, the vibratory loads on both (top and bottom) yaw bearings will be analyzed to account for interaction between the upper and lower rotor loads.

III. Rigid Booms and Tower, No Tower and Boom Shadow (Baseline)

The first load case concerns the quad-rotor turbine with rigid booms and a rigid tower with no shadow correction. This case serves as a baseline before adding complexities such as structure flexibility and tower and boom shadow correction. The peak to peak yaw bearing and boom root force components are shown in Figure 4. The vibratory forces are dominated by F_y and F_z with the force in the thrust direction, F_x, being the smallest of all the components. F_x has a lower peak to peak variation due to the combination of wind shear and gravity which is present for F_y and F_z, but not F_x. The movement of the blades is dampened in the x-direction, leading to dampened inertial loads. The sources of the F_x components are displayed in Figure 6. F_y and F_z also contain the same components just acting along their corresponding axes. The aerodynamic component is the aerodynamic force at the rotor hub. The hub inertia is the sum of the blade inertial loads. The total rotor hub force (RHF) is a load measured at the rotor hub and is made up of the vector sum of the aerodynamic and hub inertia. The nacelle force is the load measured at the attachment point of the nacelle as shown on the diagram. The boom root force is measured at the boom root. This location is at the center of the tower leading to the yaw bearing load being the sum of the boom root loads. Figures 7 and 8 shows respectively the breakdown of F_x and F_y into the peak to peak values of its components. F_x is heavily dominated by inertial loads of the blades. F_y is also dominated by blade inertia, but has a more significant aerodynamic component compared to F_x that is out of phase with the inertial load leading to the lower peak to peak value at the hub. F_z has a very similar breakdown to F_y. The vibratory loads of F_x are primarily composed of inertia from the blades flapping as opposed to being due to aerodynamics. Due to the rigid structure, the magnitude of the hub load, nacelle load, and boom root load are the same.

The time histories of the boom root and yaw bearing forces over 2 rotor rotations are shown in Figure 9. The boom root forces are in phase leading to them summing at the yaw bearing. The time histories of the boom root and yaw bearing moments are shown in Figure 10. The peak to peak values of the moment components are shown in Figure 5. From the peak to peak components, it can be seen that the moments are dominated by M_y and M_z. The boom root M_y and M_z are in phase and sum at the yaw bearing while the boom root M_x are out of phase and cancel. There is also a small difference in the magnitudes of boom root M_z. This phase difference of M_x and the magnitude difference of M_z can be explained with Figure 11 which displays the time histories of the top left boom root moments broken into the nacelle and force induced components. The nacelle moment is the moment directly transferred from the nacelle to the boom root and yaw bearing while the force induced moment is the moment generated by the nacelle forces generating a torque by acting at a distance from the yaw bearing. In Figure 11, M_y and M_z are dominated by the nacelle moments.

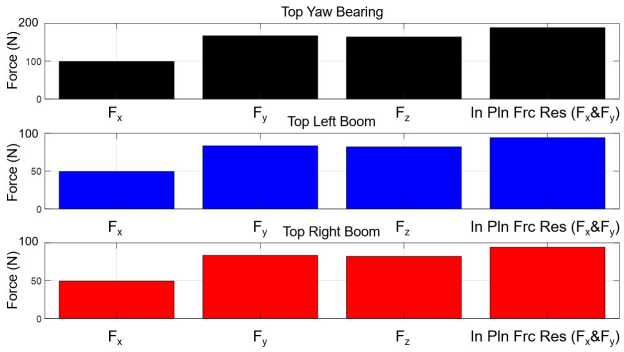

Fig. 4 Peak to Peak Values of Force Components for Top Booms

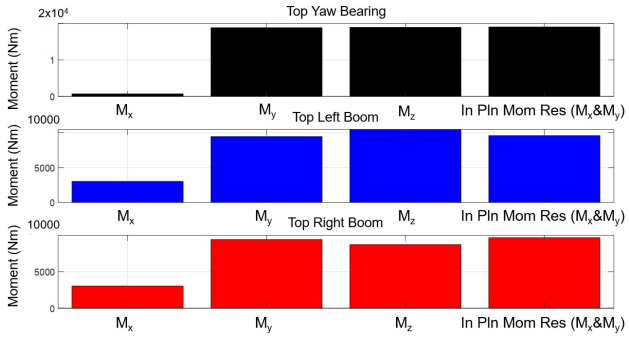

Fig. 5 Peak to Peak Values of Moment Components for Top Booms

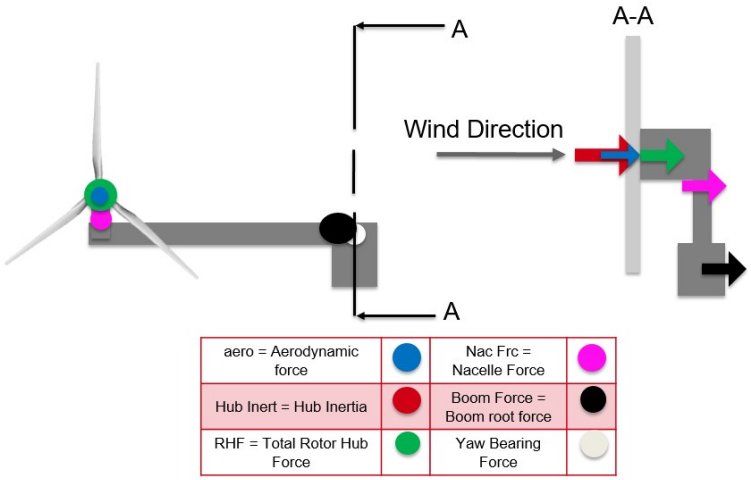

Fig. 6 F_x Component Definitions and Locations

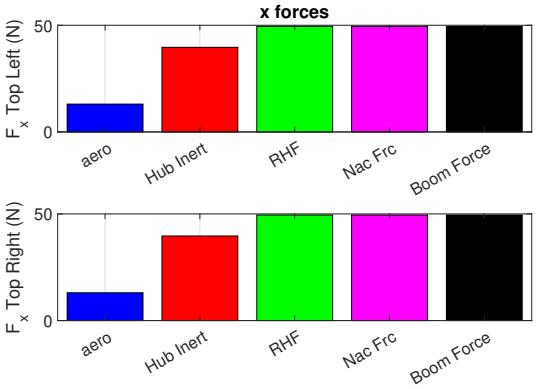

Fig. 7 Peak to Peak Values of X-Components for Top Booms

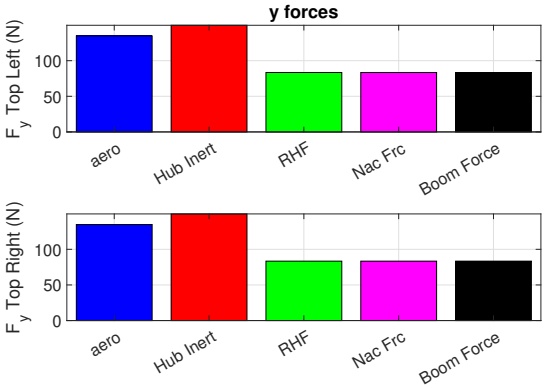

Fig. 8 Peak to Peak Values of Y-Components for Top Booms

The nacelle moments act in the same direction due to the co-rotating rotors which puts them in-phase. M_x is dominated by the force induced moment. The force induced moment of M_x is primarily F_z multiplied by the boom length. The vibratory F_z acts in phase between both rotors, but on opposite sides of the tower, leading to an out of phase force induced moment. This explains the out of phase boom root loads. The magnitude difference of the boom root M_z is

also explained by the force induced moment. The vibratory F_x acts in phase on opposite sides of the tower. For the top left boom, the force induced moment from F_x is in phase with the nacelle M_z while for the top right boom, it is out of phase causing the magnitude difference.

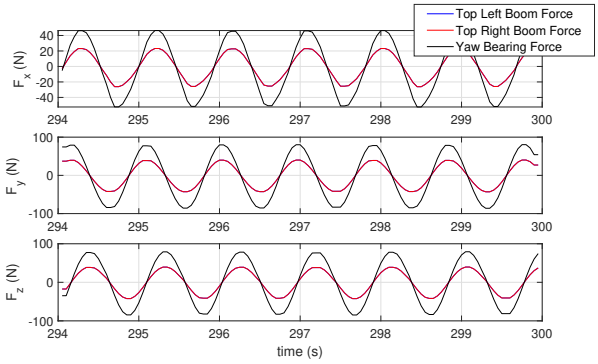

Fig. 9 Time History of Boom Root and Yaw Bearing Forces (Mean Removed)

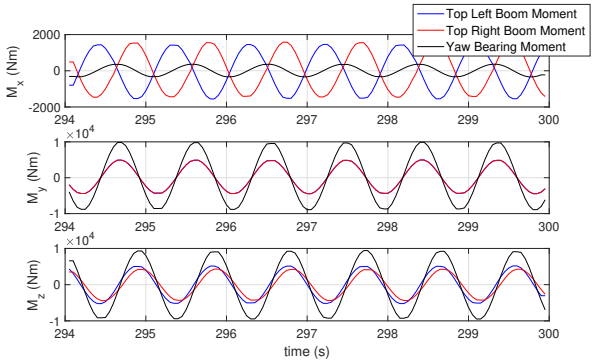

Fig. 10 Time History of Boom Root and Yaw Bearing Moments (Mean Removed)

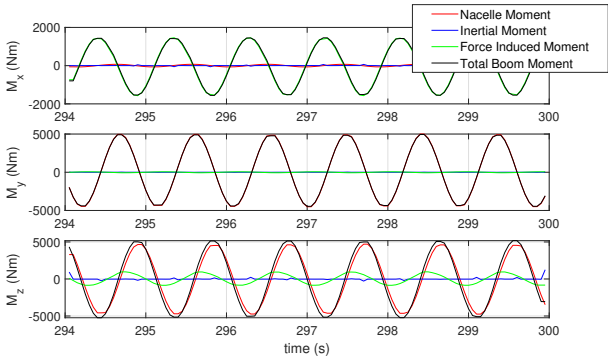

Fig. 11 Time History of Top Left Boom Root Moments Components (Mean Removed)

IV. Flexible Booms and Rigid Tower without Tower and Boom Shadow

The presence of horizontal booms are a primary difference between the structure of a single rotor and multi-rotor turbine. This next load case considers these booms and how their flexibility affects the vibratory loads. Table 2 displays the peak to peak load values and the ratio of the flexible to the rigid booms loads. The loads increase significantly from the rigid booms case indicating that there are new sources of vibratory loads that feed the magnitude change. F_x experiences the largest increase when flexible booms are considered, increasing by 25 times from the rigid booms case. F_x is now the dominant force component where in the rigid case it was the smallest. The additional loads introduced with the flexible booms are the nacelle inertia and boom inertia. Referring to Figure 12, nacelle inertia is due to motion of the large concentrated nacelle mass at the tip of the flexible boom. Boom inertia is generated by movement of the flexible boom's mass.

The breakdown of the boom root F_x and F_y loads into the load components are shown in Figures 13 and 14. The hub, nacelle, and boom inertia heavily dominate F_x, even more so than for the rigid booms case. F_y and F_z have similar component breakdowns to each other and have a large aerodynamic vibratory component similar to the rigid case. Figure 15 presents the linear x acceleration and the angular acceleration about the z-axis at the boom tip. The acceleration values are relatively small, on the order of 0.01 m/s^2, but when considering the large boom and nacelle masses (36025 kg), the inertial loads generated by the acceleration of the booms turn out to be significant as seen in the F_x component breakdown.

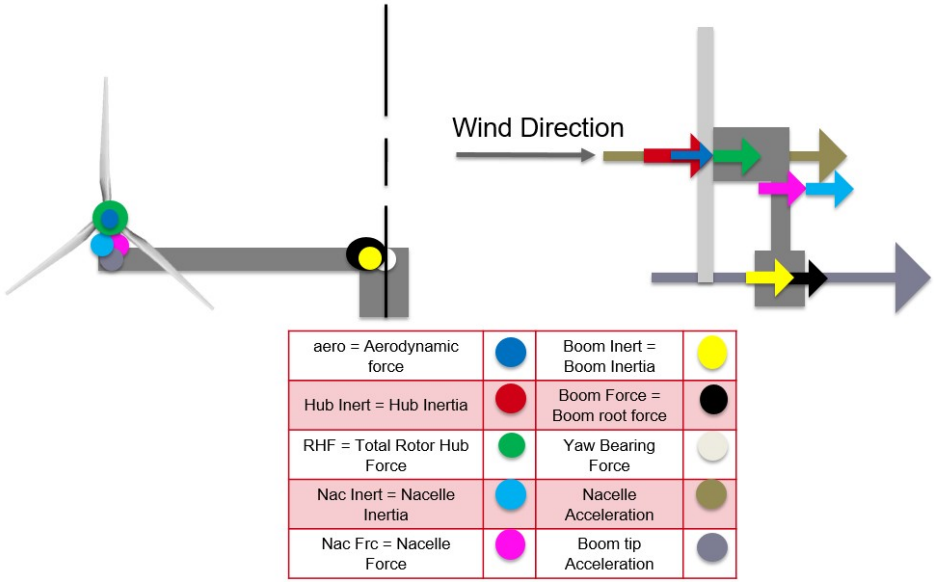

Fig. 12 F_x Component Definitions and Locations with Flexible Booms

Table 2 Peak to Peak Values of the Loads for the Flexible Booms Case

Force/Moment	Flexible Booms Peak to Peak Val	Rigid Booms Peak to Peak Val	Ratio: Flexible to Rigid
F_x	2500 N	99 N	25.3
F_y	196 N	166 N	1.18
F_z	858 N	164 N	5.23
M_x	10982 Nm	700 Nm	15.7
M_y	10046 Nm	18793 Nm	0.534
M_z	28446 Nm	18895 Nm	1.51
Force Resultant	2507 N	194 N	12.92
In-plane Moment Resultant (M_x and M_y)	13210	19780 Nm	0.791

One important point of note from Figure 13 is that the magnitudes of the left and right boom root F_x are different. The right boom root load is nearly twice the value of the left boom root load. This difference between the left and right boom root F_x loads can be explained with the gyroscopic effect. Figure 16 is used to illustrate the gyroscopic effect. In the figure, the angular momentum of the rotor (red) sums with an angular momentum generated by the nacelle mass (green). The angular momentum from the nacelle mass is due to the nacelle's center of mass being offset from the boom axis, producing a nose down pitching moment. The resultant angular momentum produced by the rotor and nacelle pitching moment is shown in orange. Due to the gyroscopic effect, the rotational system (the rotor) naturally wants to be perpendicular to the resultant angular momentum, so a gyroscopic torque, shown in blue, is generated. This torque causes a displacement of the booms, shown in yellow. This displacement also produces an acceleration which feeds into the inertial loads leading to the different boom tip accelerations seen in Figure 15. The gyroscopic torque acts in the same direction for both rotors because they are co-rotating, but the booms are mirrored on opposite sides of the tower, so the booms are displaced in opposite directions.

Load cases are run to isolate the up-down, torsion and fore-aft boom modes and combinations of the boom modes and determine which mode or combination of modes most heavily feed into the gyroscopic effect. Figure 17 display the peak to peak values for the components of F_x for each isolated boom mode and for a combination of the fore-aft

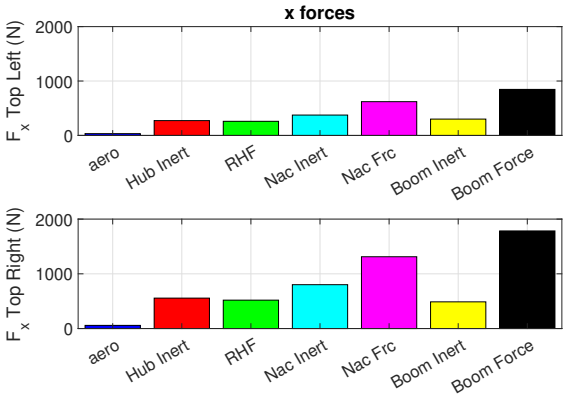

Fig. 13 Peak to Peak Values of X-Components for Top Booms

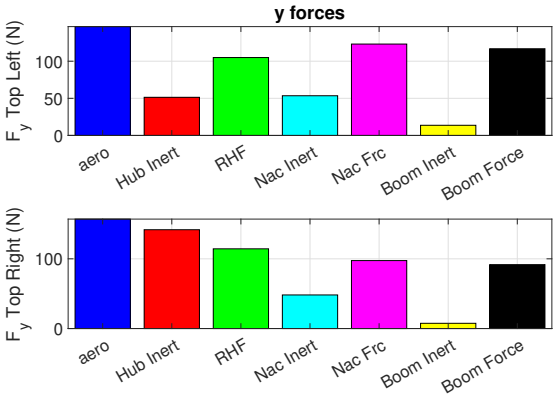

Fig. 14 Peak to Peak Values of Y-Components for Top Booms

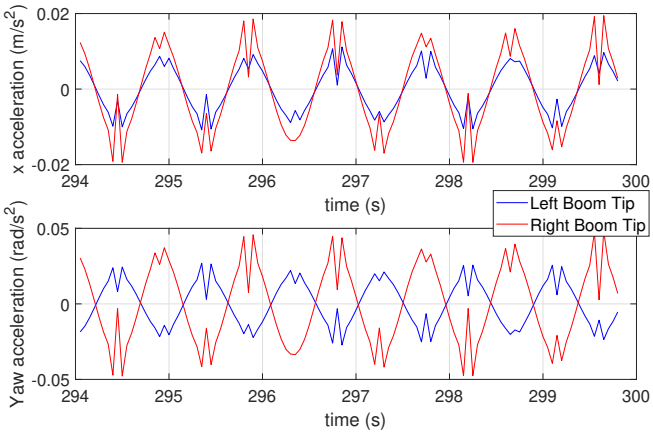

Fig. 15 Top Boom Tip Accelerations

and torsion modes. Under the effects of one mode, the difference in magnitude in F_x observed with all boom modes active is not seen. For the fore-aft and torsion modes combination, the magnitude difference between the left and right loads that is present in the all-modes case exists here. Other mode combinations do not produce this, indicating that the combination of the fore-aft and torsion modes most heavily feeds into the gyroscopic effect.

Due to the significance of the gyroscopic effect on the F_x load, it may be important to reduce the gyroscopic effect. Figures 18 and 19 show the peak to peak boom root force for co-rotating and counter-rotating rotors, respectively. The figures clearly show that the adverse gyroscopic effect can effectively be mitigated by employing counter-rotating rotors. Referring to Figure 16, if one rotor rotates in the opposite direction, the displacement direction from gyroscopic torque is reversed, making the system mirrored. This means that both booms experience the same magnitude of acceleration and any difference between the left and right inertial loads is eliminated.

The time histories of the boom root and yaw bearing moments over two rotations are displayed in Figure 20. There are notable differences between these results and the time histories with rigid booms. The vibratory load component M_z at the left and right boom are out of phase and have different magnitudes. These changes are explained with the breakdown of the top left boom root moment components in Figure 21. The time histories of M_x and M_y are similar to the rigid booms case with the introduction of an inertial moment. The dominant component of M_z is now the force induced moment produced by F_x. F_x experiences the largest increase in magnitude from the rigid to flexible booms case. This increase leads to the dominant force induced moment, which makes the boom root components out of phase as seen in M_x in Figure 10. The difference in magnitude in the F_x force components due to the gyroscopic effect feeds into the force induced moment of M_z leading to the difference in the left and right boom root M_z components observed in Figure 20.

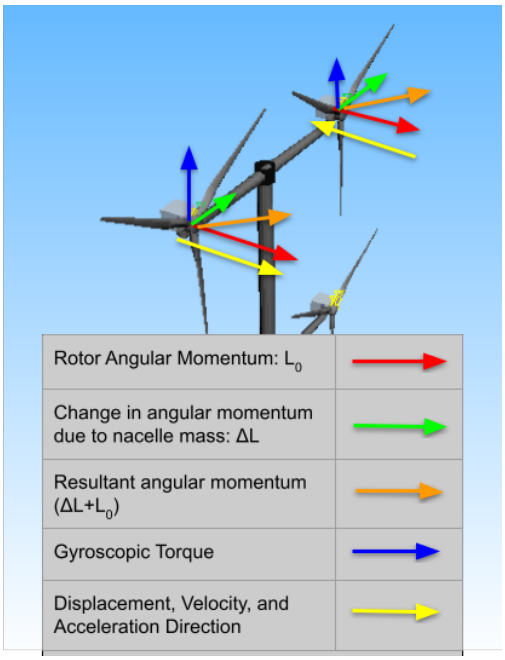

Fig. 16 Gyroscopic Effect Due to Co-Rotating Rotors

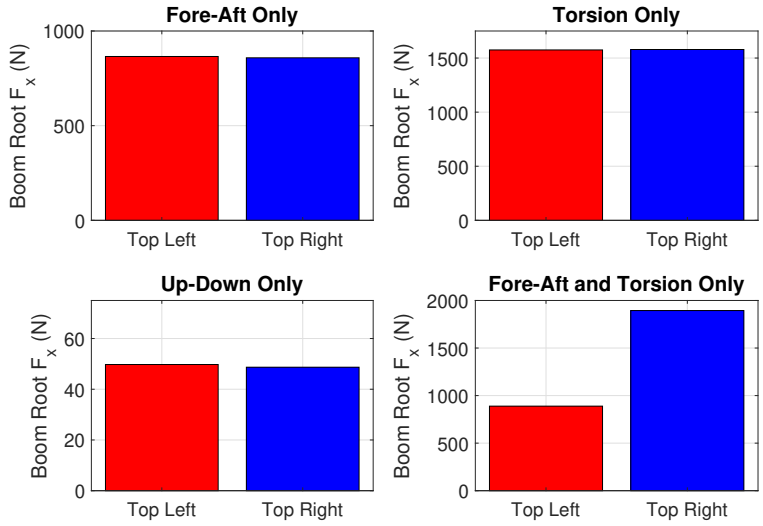

Fig. 17 Peak to Peak Thrust Force (F_x) Under Varying Boom Modes

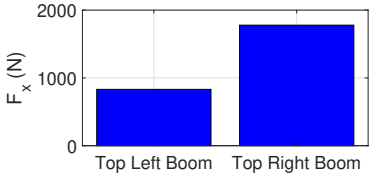

Fig. 18 Peak to Peak Values of X-Components for Co-Rotating Rotors

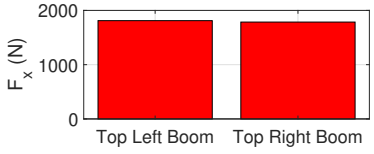

Fig. 19 Peak to Peak Values of X-Components for Counter-Rotating Rotors

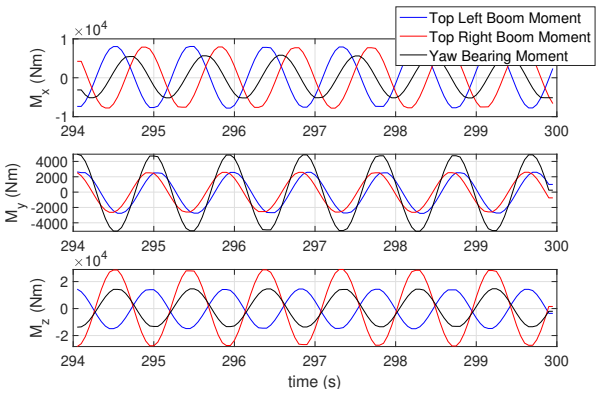

Fig. 20 Time History of Boom Root and Yaw Bearing Moments (Mean Removed)

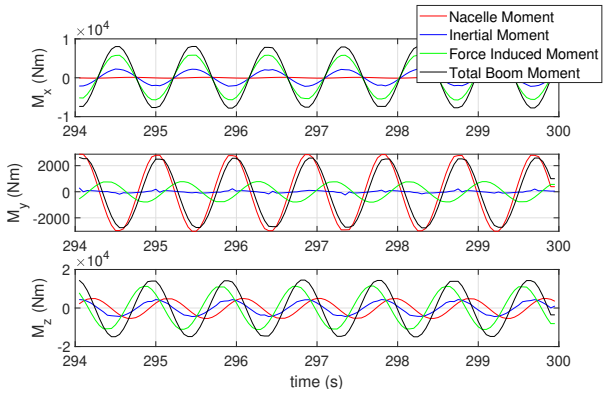

Fig. 21 Time History of Top Left Boom Root Moment Components (Mean Removed)

Due to the system being dominated by inertial loads (Fig 13), an investigation is done to see how changing the boom's specific stiffness would affect the loads. The results of this, presented in Figure 22 do not show the expected behavior of a decrease in the peak to peak F_x load with increased boom stiffness. In fact, the peak to peak load with a reduced combined boom and nacelle mass is 1.5 times that of the baseline case. When the combined boom and nacelle mass is increased, the load reduces to about 0.92x that of the baseline case. This phenomenon is explained by Table 3 which displays the natural frequencies of the boom-nacelle system and the aerodynamic excitation frequency. When the mass of the system is reduced, the natural frequency is driven closer to the aerodynamic excitation frequency, resulting in resonance. When the mass of the system is slightly increased, the natural frequency is driven away from the excitation frequency, reducing the loads. When the specific stiffness is increased by a large amount as in the last case of Figure 22, the aerodynamic excitation frequency is passed and resonance is avoided.

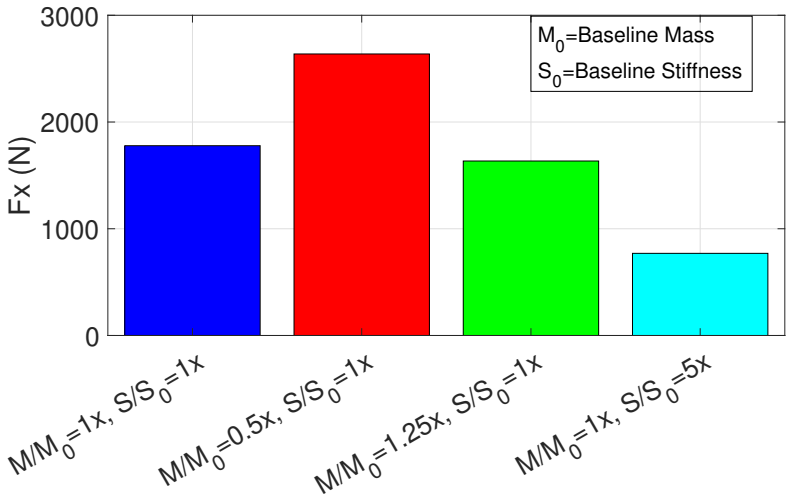

Fig. 22 F_x Peak to Peak Values Under Varying Specific Boom Stiffness

Table 3 Aerodynamic Frequency and Boom-Nacelle Natural Frequencies

Aerodynamic Excitation Frequency (3p)		
1.07-1.09 Hz		
Stiffness	Mass	Fore-aft Pitch Mode
1x	1x	0.9754 Hz
	0.5x	1.0346 Hz
	1.25x	0.9613 Hz
5x	1x	3.2719 Hz

V. Flexible Booms, Rigid Tower, Tower and Boom Shadow

Next, tower and boom shadow is included (in addition to flexible booms) during the load analysis. The correction for shadow was made using Equation 1. Figure 23 shows the inflow, corrected for tower and boom shadow, for the top left and right rotors. Tower and boom shadow affects the axial components of the wind as it passes around the boom; leading to an impulse in the velocity and the aerodynamic loads (Figure 24). The combination of co-rotating rotors and mirrored tower and boom shadow (with respect to the tower) results in a different magnitude and phase in the loads from tower and boom shadow.

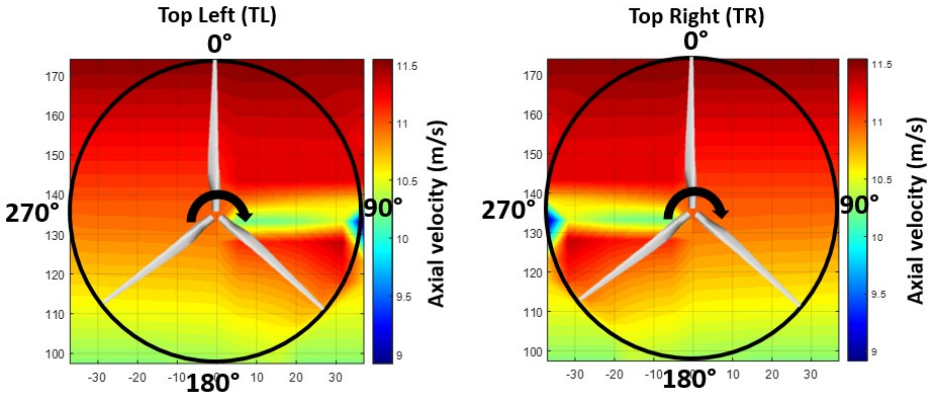

Fig. 23 Rotor Wind Fields Under the Effect of Tower and Boom Shadow

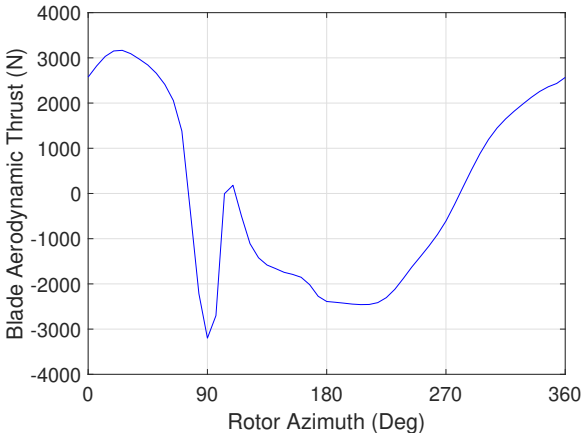

Fig. 24 Single Blade Aerodynamic Force Under the Effect of Tower and Boom Shadow (Mean Removed)

Figure 25 displays the F_x load at the top left rotor hub in the frequency domain. When shadow is considered, the magnitude of the 3p load is significantly increased. This increase in the loads carries over to the other 3p multiples (6p, 9p, etc.) which are more than 2 orders of magnitude larger than the case without shadow. The effect of the boom shadow resembling an impulse perturbation to the incoming wind, resulting sudden variation in the aerodynamic load as the blade passes the booms (see Figure 24), is an increase in the higher frequency loads. The aerodynamic loading of a blade has a large negative spike at an azimuth angle of around 90 degrees, which corresponds to the blade passing over the boom and through the shadow. This spike is the dominant factor in the high frequency loads.

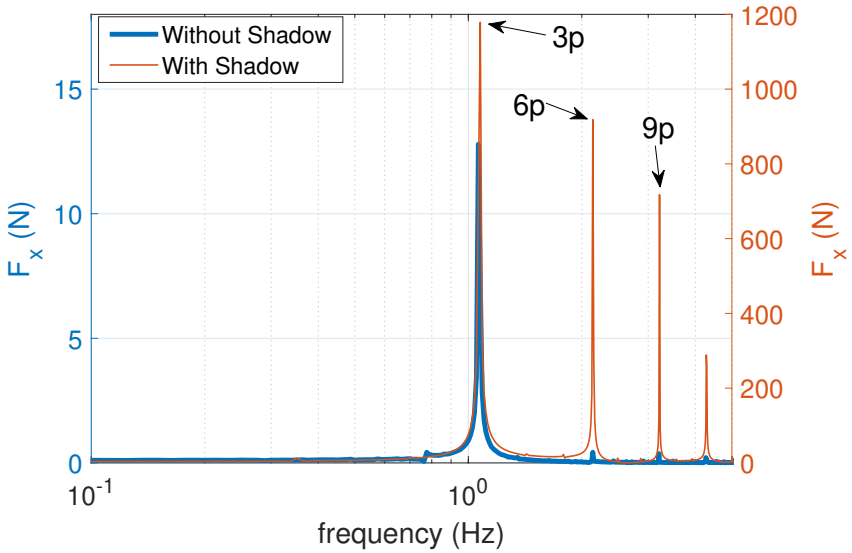

Fig. 25 F_x of Top Left Rotor Hub In Frequency Domain with/without Tower and Boom Shadow

Figures 26 and 27 display the peak to peak values of the different load components on the top booms. The main point of note for the vibratory load in the thrust direction (F_x) is the increase in the aerodynamic component from the previous case. The change in the aerodynamic component and results in the frequency domain indicate that tower and boom shadow is the dominant effect when it is considered. Table 4 lists the peak to peak values of the loads for the tower and boom shadow and no shadow cases and the ratio between them. The presence of tower and boom shadow increases all the vibratory loads. This increase ranges from an increase of 3x to an increase of over 10x for F_y and M_x.

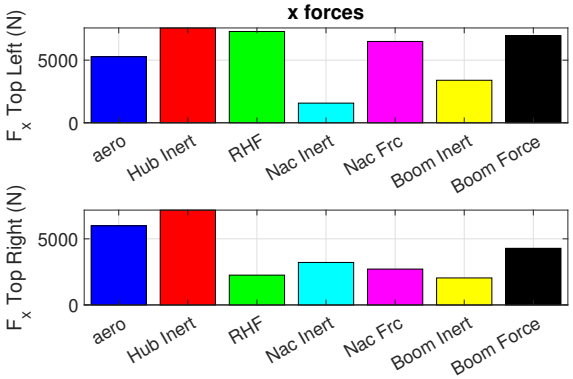

Fig. 26 Peak to Peak Values of X-Components for Top Booms

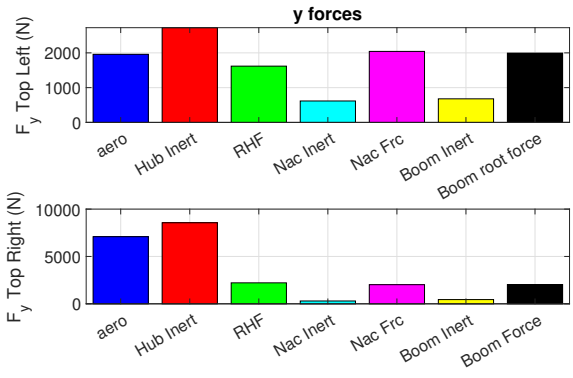

Fig. 27 Peak to Peak Values of Y-Components for Top Booms

Tower and boom shadow has a significant effect on the vibratory loads of the turbine; significantly increasing the high frequency contents (6p, 9p, etc.) of the vibratory loads. The tower and boom shadow is tied to the aerodynamic

Table 4 Peak to Peak Values of the Loads for the Boom and Tower Shadow Case

Force/Moment	Shadow Peak to Peak Val	No Shadow Peak to Peak Val	Ratio: Shadow to No Shadow
F_x	7764 N	2500 N	3.11
F_y	2151 N	196 N	10.97
F_z	5797 N	858 N	6.76
M_x	110866 Nm	10982 Nm	10.1
M_y	38981 Nm	10046 Nm	3.88
M_z	166396 Nm	28446 Nm	5.85
In-plane Force Resultant (F_x and F_y)	8056 N	2507 N	3.21
In-plane Moment Resultant (M_x and M_y)	138677 Nm	13210 Nm	10.5

shape and size of the boom, so changes to the aerodynamic shape and size of the boom will change the boom shadow. Figure 28 displays velocity deficit of the incoming wind at the rotor plane due to the presence of a boom with varying diameter. As the boom diameter is decreased, the effect of shadow on the axial flow decreases. This feeds into the vibratory loads. Figure 29 shows the F_x load in the frequency domain of the top left hub rotor hub at different boom diameters. When the boom diameter is reduced to 80%, the hub 3p load decreases by 39% and when the boom diameter is reduced to 60%, the 3p hub load decreases by 66%. The implication here is that large reductions in the vibratory loads can be achieved by making making changes to the boom that reduce the effect of the boom shadow.

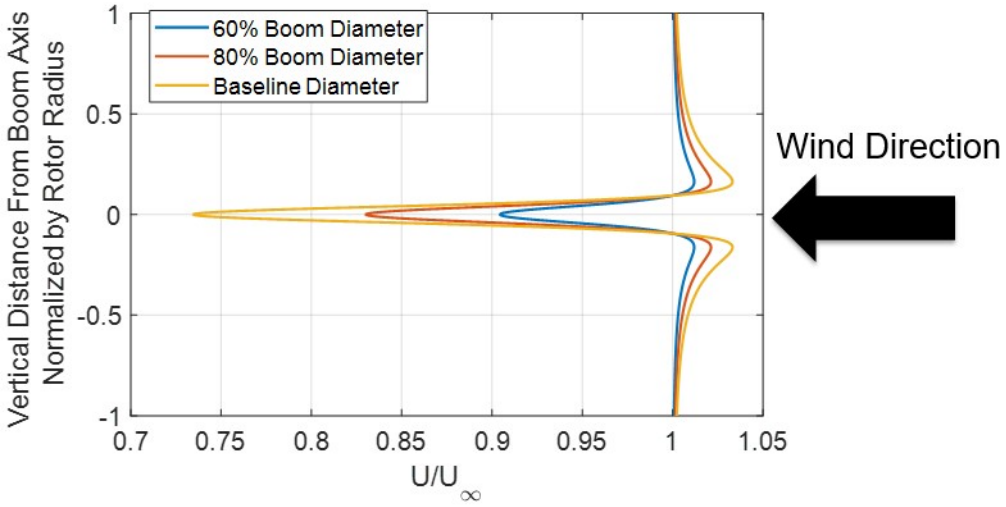

Fig. 28 U/U_∞ at Rotor Plane Under Effect of Boom Shadow

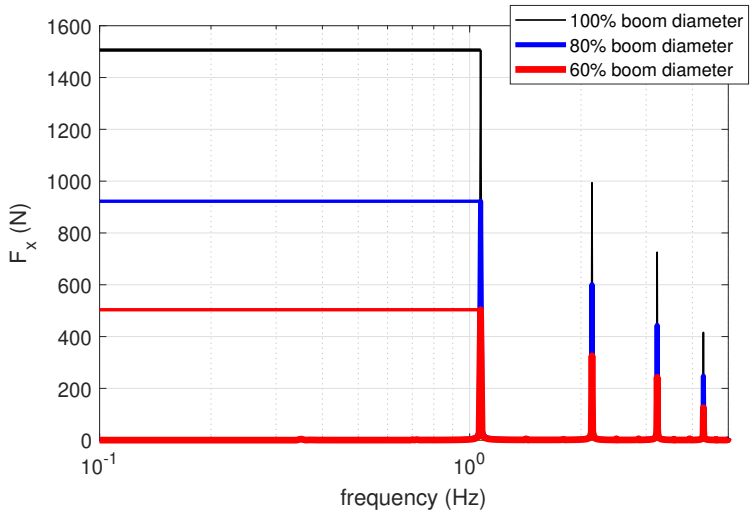

Fig. 29 FFT of Top Left Hub F_x With Varying Boom Diameter

VI. Flexible Tower and Booms, Tower and Boom Shadow

To account for all vibratory components, tower flexibility must be enabled as the tower generates inertial loads and couples the dynamics of the top and bottom rotors. Table 5 lists the peak to peak values of the top and bottom yaw bearings vibratory loads as well as the ratio between the flexible and rigid tower loads. Tower flexibility increases all the vibratory load components, but has the most significant effect on F_y. The increased magnitude of the loads is due to interaction between the top and bottom yaw bearing loads and tower inertia. The vibratory loads at the bottom bearing are larger than the upper loads due to the higher wind shear gradient across the bottom rotors (compared to the top rotors). The wind velocity under different wind shear exponents is shown in Figure 30. The gradient is larger for the bottom rotors for all wind shears that are in between one and zero resulting in larger vibratory loads.

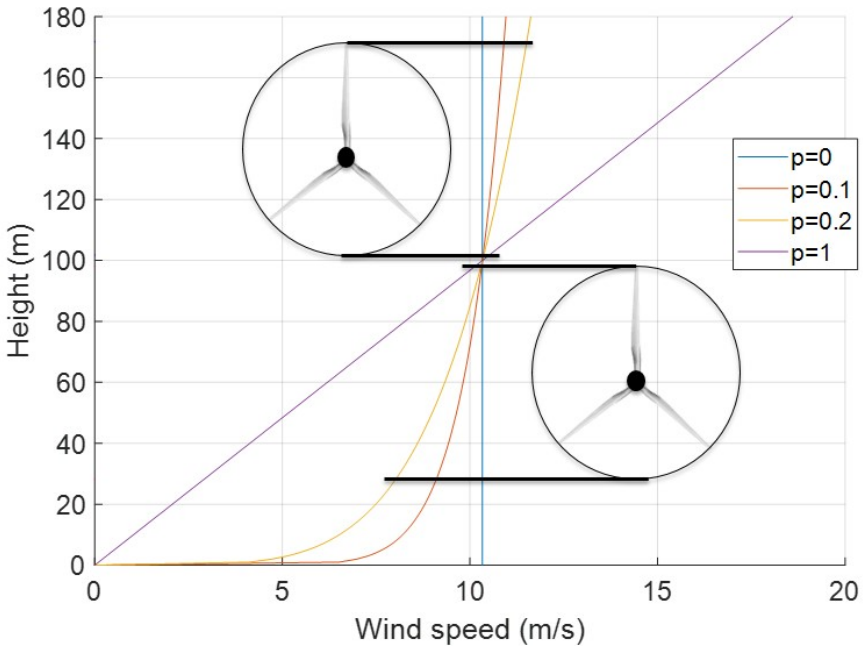

Fig. 30 Wind Velocity Under Varying Wind Shear Exponents (p = Wind Shear Exponent)

Table 5 Peak to Peak Values of the Loads for a Flexible Tower

Force/Moment	Top Yaw Bearing Peak to Peak Val	Bot Yaw Bearing Peak to Peak Val	Ratio: Flexible to Rigid Tower
F_x	10254 N	16167 N	1.32
F_y	6951 N	6450 N	3.23
F_z	9491 N	23062 N	1.64
M_x	178170 Nm	203302 Nm	1.61
M_y	89840 Nm	128460 Nm	2.30
M_z	290570 Nm	564070 Nm	1.75
In-plane Force Resultant (F_x and F_y)	12388 N	17406 N	1.54
In-plane Moment Resultant (M_x and M_y)	199540 Nm	240490 Nm	1.44

Figure 31 shows the time histories and the loads in the frequency domain for the vibratory F_x and F_y of the top and bottom yaw bearings. Looking at the time histories of the forces, it can be seen that there is a low frequency signal underneath the 3p and high frequency loading. This low frequency signal is dominant in F_y, leading to why the magnitude of the load increased from the rigid tower case more so than for the other loads. The low frequency signal (0.1501 Hz) also occurs at a frequency close to the side-side mode of the tower which is not dampened by aerodynamics. This side-side mode occurs at 0.1509 Hz. The explanation for the low frequency signal lies in the interaction between the top and bottom yaw bearing loads. The top and bottom rotors rotate at different speeds due to the different average wind speeds from wind shear. Due to the top rotors' speeds, the aerodynamic excitation frequency is at 1.07 Hz (see Figure 25. The bottom rotors operate at a slightly slower speed resulting in an aerodynamic excitation frequency of 0.915 Hz. The frequency domain results show that components of the F_x and F_y loads are at these two frequencies. There is also a low frequency peak that corresponds to the low frequency signal present in the time histories. This signal is a beat frequency resulting from the incoming top and bottom loads acting at different frequencies. It is also of note that the bottom frequency is dominant for the top and bottom yaw bearing loads. This can be attributed to the higher load values due to wind shear and due to possible resonance effects between the bottom rotors and the structure modes. The modes of interest are detailed in Table 6. These modes of interest have frequencies close to the 3p excitation frequencies of the rotors. The modes at 0.88 and 0.93 Hz fall closer to the bottom excitation 3p frequency than any of the other modes do to the top. Similar to what occurred with the boom loads and the top excitation frequency in Figure 22, the tower frequencies are resonating with the bottom loads leading to an increase in the peak to peak value at that frequency and resulting in the dominance of the bottom loads at the yaw bearings.

Table 6 Excitation Frequencies and Structure Modal Frequencies

Top Excitation Frequency (3p)	1.07 Hz
Bot Excitation Frequency (3p)	0.915 Hz
Structure Modes	**Frequency (Hz)**
Tower side-side, boom up-down	0.885
Tower and boom fore-aft, pitch	0.935
Boom fore-aft, pitch	0.97
Tower and boom fore-aft	1.12

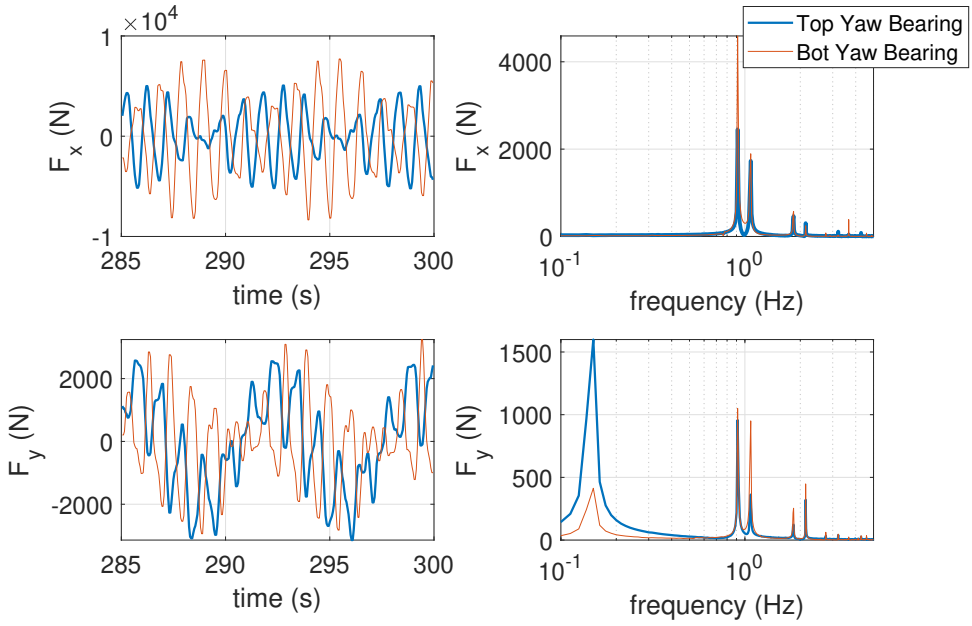

Fig. 31 Time Histories of Yaw Bearing Forces and Loads in Frequency Domain (Mean Removed)

VII. Conclusion

A load component analysis is performed on the support structure (tower and booms) of a quad-rotor wind turbine, considering a combination of support structure flexibility and environmental conditions (wind shear, tower and boom shadow). The resulting key takeaways are:

- The gyroscopic effect leads to a dissimilarity in the magnitude between the left and right loads in the case of co-rotating rotor operation and when boom flexibility is accounted for. This difference in magnitude most heavily affects loads in the thrust direction (F_x).
- The inertial loads are more dominant than the aerodynamic loads. Structural inertial loads dominate the system due to the large nacelle masses mounted at the boom tip and the inertia of the flexible booms.
- Tower and boom shadow increases the magnitude of the vibratory load and introduces higher load harmonics (6p, 9p, etc.). The effect of tower and boom shadow can be reduced significantly by changing the boom size or aerodynamic shape with results in lowering the magnitude of the tower and boom shadow.
- Considering rigid tower, the top and bottom yaw bearing loads decoupled such that only load present on the yaw bearing is from the respective rotors. In the case of a flexible tower, the loads of the top and bottom yaw bearings are coupled resulting in the aerodynamic excitation from the top and bottom rotors observed at both yaw-bearings. The top and bottom loads, present at both yaw bearings, are at different frequencies due to the rotors operating at different speeds.
- The beat frequency, resulting from the top and bottom rotors operating at rotors speeds close to each other, causes resonance of the side-side tower mode since this mode has low aerodynamic damping.
- The mass and stiffness distribution of the booms and tower needs to be designed with a strong focus on avoiding resonance with excitation (load) frequency from the rotors.

Acknowledgments

This study was funded by the New York State Energy Research and Development Authority (NYSERDA) and General Electric (GE) Renewables under Award No.127346, Quad-Rotor Wind Turbine, with Mr. Scott Larsen (NYSERDA), Mr. Peter Maxwell (GE) as the Program Managers. Their support is gratefully acknowledged. NYSERDA and GE have not reviewed the information contained herein, and the opinions expressed in this report do not necessarily reflect those of NYSERDA or GE.

References

[1] Holst, H., "Opfindelsernes Bog,Nordisk Forlag," 1923.

[2] Honnef, H., "Windkraftwerke, Vieweg," 1932.

[3] Jamieson, P., and Hassan, G., *Innovation in wind turbine design*, Vol. 2, Wiley Online Library, 2011.

[4] Laan, M. P. v. d., Andersen, S. J., Ramos García, N., Angelou, N., Pirrung, G. R., Ott, S., Sjöholm, M., Sørensen, K. H., Vianna Neto, J. X., Kelly, M., et al., "Power curve and wake analyses of the Vestas multi-rotor demonstrator," *Wind Energy Science*, Vol. 4, No. 2, 2019, pp. 251–271.

[5] Ghaisas, N. S., Ghate, A. S., and Lele, S. K., "Large-eddy simulation study of multi-rotor wind turbines," Vol. 1037, 2018, p. 072021. https://doi.org/10.1088/1742-6596/1037/7/072021, URL https://doi.org/10.1088/1742-6596/1037/7/072021.

[6] Bastankhah, M., and Abkar, M., "Multirotor wind turbine wakes," *Physics of Fluids*, Vol. 31, No. 8, 2019, p. 085106. https://doi.org/10.1063/1.5097285.

[7] Chasapogiannis, P., Prospathopoulos, J. M., Voutsinas, S. G., and Chaviaropoulos, T. K., "Analysis of the aerodynamic performance of the multi-rotor concept," Vol. 524, 2014, p. 012084. https://doi.org/10.1088/1742-6596/524/1/012084, URL https://doi.org/10.1088/1742-6596/524/1/012084.

[8] Ohya, Y., Miyazaki, J., Göltenbott, U., and Watanabe, K., "Power Augmentation of Shrouded Wind Turbines in a Multirotor System," *Journal of Energy Resources Technology*, Vol. 139, No. 5, 2017. https://doi.org/10.1115/1.4035754.

[9] Ferede, E., and Gandhi, F., "Modal Analysis of a Quad-Rotor Wind Turbine," *Journal of Physics: Conference Series*, Vol. 1618, 2020, p. 032002. https://doi.org/10.1088/1742-6596/1618/3/032002.

[10] *Operational Modal Analysis of a Multi-Rotor Wind Turbine*, International Ocean and Polar Engineering Conference, Vol. All Days, 2019.

[11] Filsoof, O. T., Yde, A., Bøttcher, P., and Zhang, X., "On critical aeroelastic modes of a tri-rotor wind turbine," *International Journal of Mechanical Sciences*, Vol. 204, 2021, p. 106525. https://doi.org/https://doi.org/10.1016/j.ijmecsci.2021.106525, URL https://www.sciencedirect.com/science/article/pii/S0020740321002605.

[12] Ferede, E., and Gandhi, F., "Aeroelastic Analysis of a Quad-Rotor Wind Turbine," *Wind Energy*, 2021, pp. 1–18. https://doi.org/10.1002/we.2681.

[13] Spagnolo, F., Papageorgiou, D., Galeazzi, R., Thomsen, J. S., and Sørensen, K. H., "Extremum Seeking Control for Multi-Rotor Wind Turbine in the Full-Load Region," *IFAC-PapersOnLine*, Vol. 53, No. 2, 2020, pp. 5386–5391. https://doi.org/https://doi.org/10.1016/j.ifacol.2020.12.1525, 21st IFAC World Congress.

[14] Rulka, W., "SIMPACK—A computer program for simulation of large-motion multibody systems," *Multibody systems handbook*, Springer, 1990, pp. 265–284.

[15] Jonkman, J. M., Hayman, G., Jonkman, B., Damiani, R., and Murray, R., "AeroDyn v15 user's guide and theory manual," *NREL Draft Report*, 2015.

[16] Dykes, K. L., and Rinker, J., "Windpact reference wind turbines," Tech. rep., National Renewable Energy Lab.(NREL), Golden, CO (United States), 2018.